Rutile TiO₂ Nanosheet Arrays Planted on Magnetron Sputtered Ti Metal Layers for Efficient Perovskite Solar Cells

Nan Zhang[1a], Meidan Ye[1a], Xiaoru Wen[1], Changjian Lin[1,2*]

(1. *State Key Laboratory of Physical Chemistry of Solid Surfaces, and Department of Chemistry,*
College of Chemistry and Chemical Engineering, Xiamen University, Xiamen 361005, *China*;
2. *Research Institute for Biomimetics and Soft Matter, Fujian Provincial Key Lab for*
Soft Functional Materials Research, Department of Physics, College of Physical Science and
Technology, Xiamen University, Xiamen 361005)

Abstract：In this work, vertical rutile titanium oxide (TiO₂) nanosheet arrays (NSAs) were firstly hydrothermally grown on the top of thin titanium (Ti) metal layers which were loaded on fluorine doped tin oxide (FTO) substrates by the DF magnetron sputtering deposition method. After an annealing post-treatment, the Ti metal layers were transformed into the compact TiO₂ layers with a strong connection between the rutile TiO₂ NSAs and the FTO substrates. For comparison, the rutile TiO₂ NSAs were similarly planted over two compact TiO₂ layers fabricated through atomic layer deposition (ALD) and spin coating (SC) methods, respectively. When served as the scaffold layers in perovskite solar cells (PSCs), the Ti-based TiO₂ NSAs showed the best cell performance due to the high quality of the TiO₂ NSA nanostructure and excellent interface contacts among the TiO₂ NSAs/TiO₂ compact layers/FTO substrate interface. Significantly, a highest cell efficiency of 11.82% was obtained after careful modification on the organization procedures for the PSC devices.

Key words: Ti metal layer; TiO₂ nanosheet arrays; perovskite solar cells

CLC Number：O646

Document Code：A

Nowadays, exploring renewable energy has become an increasingly urgent task owing to the energy crisis over fossil fuel supplies and sustainability in the future. Photovoltaic technology represents the most promising strategy to overcome this problem[1]. Recent development in organic-inorganic halide perovskite solar cells (PSCs) has shown great potential for large-scale application owing to the outstanding power conversion efficiency (PCE), simple preparation procedure and low material cost[2-9]. Since the first report of methyl ammonium lead halide, $CH_3NH_3PbX_3$ (X = Br, I), sensitized liquid solar cells in 2009[10], the PCEs of PSCs have jumped from 3.8% to over 22% of the all solid-state solar cells now[11]. Over the past few years, extensive investigation has been carried out, including optimizing the perovskite films[12-21], modulating the blocking and scaffold layers[22-26], modifying the HTM layers and engineering the interface/bandgap in PSCs[27-33], in order to further develop highly efficient solid-state solar cells at low cost and high stability.

As the most common device configuration for PSCs, a porous PSC usually adopts a compact TiO₂ layer onto a pre-cleaned conductive substrate which acts as a blocking layer to prevent direct contact between the conductive substrate and the infiltrated HTM layer[34-35], and a nanostructured TiO₂ scaffold layer loaded on the compact TiO₂ layer to assist the

perovskite film deposition and transport photo-gener ated electrons from perovskite sensitizers[34,36-37]. Several strategies have been developed to construct a compact TiO$_2$ layer on the conductive substrate, including spin-coating[38-39], spray pyrolysis deposition[23,40], atomic layer deposition (ALD)[41-42], and magnetron sputtering[43-44]. With regard to the TiO$_2$ scaffold layer, a mesoporous TiO$_2$ layer is one of the most popular choices which can be deposited by spin-coating, screen-printing or doctor blading the TiO$_2$ nanoparticle (NP) paste on the top of the compact TiO$_2$ blocking layer followed by a sintering process[45-49]. In addition to TiO$_2$ NPs, one-dimensional (1D) TiO$_2$ nanostructures such as nanowires (NWs)/nanorods (NRs)[50-57], nanotubes (NTs)[58-59], nanofibers(NFs)[60], and nanocones (NCs)[61], 2D TiO$_2$ nanosheets (NSs)[62-63], and complicated 3D TiO$_2$ materials[64-67], have been also used in PSCs owing to their special properties, including high-speed conduction path way or large surface area. The relevant studies of 2D TiO$_2$ NSs for a scaffold layer in PSCs are seldom till now, and the anatase phase is usually the preferences due to its high activity of the exposed (001) facet benefiting to the interfacial properties between the perovskite and the electron collector[62-63]. For example, Han et al. employed a double layer of TiO$_2$ NSs containing high levels of exposed (001) facets and ZrO$_2$ as a scaffold in a hole-conductor-free fully printable porous PSCs with a PCE of 10.64%[62]. Besides, Dar et al. developed a TiO$_2$ scaffold composed of (001)-oriented nanoplatelets of anatase TiO$_2$ for PSCs with a PCE of 12.30%[63]. However, the rutile TiO$_2$ NSAs grown on transparent conductive substrates as the scaffold materials in PSCs have not been reported in the literatures.

Herein, the oriented rutile TiO$_2$ NSAs were hydrothermally grown on a thin Ti metal layer which was deposited on a FTO substrate by the DF magnetron sputtering method. Subsequently, a 450 ℃ annealing process was used to improve the crystallinity of the rutile TiO$_2$ NSAs. And more importantly, such heating treatment simultaneously converted the metallic Ti surface into a compact TiO$_2$ layer which was well contacted with the rutile TiO$_2$ NSAs. Compared to the rutile TiO$_2$ NSAs directly formed on the compact TiO$_2$ layers prepared via ALD and spin coating (SC) methods, the Ti-based rutile TiO$_2$ NSAs presented superior performance when they were applied as scaffold layers in PSCs, mainly due to the compact TiO$_2$ layer directly thermally converted from the sputtered Ti metal layer, which possessed well connection with the orderly rutile TiO$_2$ NSAs. Upon optimization of the rutile TiO$_2$ NSAs and other device preparation processes, the PCE value of the PSCs reached up to 11.82%.

1 Experimental

1.1 Deposition of Ti Metal and Compact TiO$_2$ Layers on FTO Substrates

Fluorine doped tin oxide (FTO) substrates were successively cleaned by acetone, ethanol and deionized (DI) water, and dried in an oven. DF magnetic sputtering loaded with a Ti target (99.995%) was used as the source to deposit a Ti thin layer with thickness of ~ 50 nm on the cleaned FTO substrate under a power of 144 W for 5 min, which was then washed with ethanol and dried by N$_2$ gas. Compact TiO$_2$ layers were obtained via atomic layer deposition (ALD) and spin coating (SC) methods, respectively. For the ALD method[68], the compact TiO$_2$ layer with thickness of ~ 30 nm was deposited on the cleaned FTO substrate in pulse mode with a nitrogen flow at 200 ℃ using tetrakis (dimethylamino) titanium (TDMAT) and H$_2$O as Ti and O precursors, respectively. The deposited TiO$_2$ layer was annealed under 500 ℃ for 30 min. For the SC method[23], the compact TiO$_2$ layer with thickness of ~ 80 nm was spin coated on the cleaned FTO substrate at 1500 r·min^{-1} for 40 s using the *n*-butanol solution of titanium diisopropoxidebis (acetylacetonate) as TiO$_2$ precursor. The above film was heated at 125 ℃ for 5 min, and then the same spin-coating process was repeated. The final film was heat-treated at 500 ℃ for 30 min.

1.2 Growth of Rutile TiO$_2$ NSAs on the Pre-Treated FTO Substrates

The above-mentioned Ti and TiO$_2$-loaded FTO substrates were then separately placed in 60 mL aqueous solution (pH = 0.85) with TiCl$_3$ (0.8 mL 15

wt% of $TiCl_3$ in H_2O and HCl solution) at a 45° angle against the wall of the Teflon-lined stainless steel au toclave (100 mL) with their conducting side facing down. The hydrothermal reaction was performed at 80 °C for 4 h in an oven. The autoclave was then cooled to room temperature in air. Subsequently, the FTO substrates were taken out, rinsed extensively with DI water, dried in air and finally annealed at 450 ℃ for 2 h. The effects of growth parameters, including initial concentrations of precursor and solution acidity, on the resulting structures of the Ti-loaded FTO substrates were systematically investigated. Before organized into the PSC devices, the prepared TiO_2 films were placed in 0.2 mol·L^{-1} $TiCl_4$ aqueous solutions at 70 °C for 0.5 h. After rinsing with DI water and drying in an oven, the $TiCl_4$-treated sample was annealed at 450 °C for 30 min again.

1.3 Organization of PSC Device Based on the Rutile TiO_2 NSAs

The $CH_3NH_3PbI_{3-x}Cl_x$ perovskite was deposited on the TiO_2 NSAs in glove box or air condition (humidity: 60 ~ 70%) by one-step spin coating (2000 r·min^{-1}, 30 s) from a 40wt% mixed solution of $PbCl_2$ and CH_3NH_3I in N, N-dimethylformamide ($PbCl_2$: CH_3NH_3I = 1:3), and then heated at 100 °C for 2 h on a hot plate for crystallization of perovskite. Subsequently, the as-prepared perovskite film with dark brown color was spin coated (4000 r·min^{-1}, 30 s) 0.06 mol·L^{-1} 2,2',7,7'-tetrakis (N,N-di-4-methoxyphenylamino)-9, 9'-spirobifluorene (spiro-OMeTAD) as the hole transporting material (HTM) after it cooled to room temperature. The HTM solution was prepared by dissolving 72.3 mg spiro-OMeTAD in 1 mL cholobenzene and then adding 17.5 μL 520 mg·mL^{-1} lithium bis-(trifluoromethylsyfonyl)imide salt (Li-TFSI) and 28.8 μL tert-butylpyridine (t-BP) as a dopant and an additive, respectively. The devices were then stored in a desiccator in the dark for 12 h. 80 nm-thick Au back contact was deposited on the spiro-OMeTAD layer by vacuum and thermal evaporation technique[24]. The active surface area of PSCs was 0.09 cm^2.

For comparison, the perovskite films were also deposited in glove box by two-step dipping/spin coating methods, respectively. For the two-step dipping method, 1 mol·L^{-1} PbI_2 in N,N-dimethylformamide was firstly pre-heated at 70 ℃, and then spin-coated (5000 r·min^{-1}, 30 s) on the TiO_2 NSAs, followed by a heating treatment at 70 ℃ for 30 min. After cooled to room temperature, the samples were firstly immersed in isopropanol for 2 s, then dipped in 0.038 mol·L^{-1} CH_3NH_3Cl for 20 s, and finally heated at 70 ℃ for 30 min. For the two-step spin coating method, 1 mol·L^{-1} PbI_2 in N,N-dimethylformamide was similarly pre-heated at 70 ℃, and then spin-coated (5000 r·min^{-1}, 30 s) on the TiO_2 NSAs, followed by a heating treatment at 70 ℃ for 30 min. After cooled to room temperature, 0.038 mol·L^{-1} CH_3NH_3Cl in isopropanol was spin coated (4000 r·min^{-1}, 20 s) on the above samples which were finally heated at 100 ℃ for 10 min.

1.4 Characterization

The morphologies of samples were observed by field emission scanning electron microscope (FESEM, HITACHI S-4800) and transmission electron microscope (TEM, JEOL JEM-2100) with an accelerating voltage of 200 kV. An SEM equipped with an energy dispersive X-ray spectrometer (EDS) was used to analyze the composition of samples. Phase identification of materials was examined by X-ray diffraction (XRD, Panalytical X'pert PRO). Performance of the resulting PSCs was obtained by measuring photocurrent density-photovoltage (*J-V*) curves under AM 1.5G simulated solar light (Oriel 300 W Xe lamp and Newport AM-1.5G filter). The incident-photon-to-current efficiency (IPCE) spectra as a function of wavelength (λ= 300 to 800 nm) were measured by a monochromator (Oriel, Model: 74125).

2 Results and Discussion

Firstly, a Ti metal layer with the thickness of ~ 50 nm (Figure 1B) was deposited on a FTO substrate (Figure 1A) via the DF magnetron sputtering method, accompanying by the color transformation of the substrate from transparent (the inset in Figure 1A) to brown green (the inset in Figure 1B). Besides, the feature of the FTO substrate surface was not changed much and the loading of the thin Ti metal layer only

made it smooth (Figure 1B). For comparison, the compact TiO_2 layers prepared by ALD (film thickness $\sim$ 30 nm) and SC (film thickness $\sim$ 80 nm) methods both with a 500 °C-heating post-treatment are shown in Figure 1C and Figure 1D, respectively. It was found that the compact TiO_2 layer formed by ALD presented irregular granular shape on the FTO substrate with light-yellow color (the inset in Figure 1C). While the compact TiO_2 layer made by the SC method was composed of numerous nanoparticles with the diameter of $\sim$ 10 nm and the color of the de-
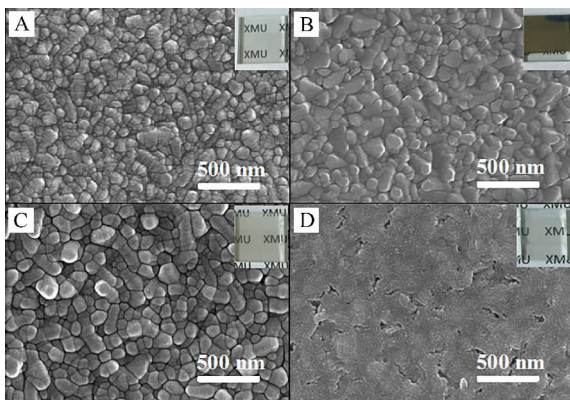

Fig. 1 SEM images of top view of the pure FTO substrate (A), Ti metal layer (B), ALD-prepared (C) and SC-prepared (D) compact TiO_2 layers on FTO substrates. Insets are their corresponding real photos.

posited substrate remained transparent (the inset in Figure 1D).

As shown in Figure 2A, the XRD patterns of the Ti metal layer from the sputtering process, and compact TiO_2 layers from the ALD and SC methods all exhibited the similar peaks to that of the pure FTO substrate because these films were too thin and the characteristic XRD peaks of the FTO substrate were too strong. However, when the TiO_2 NSAs were grown on these Ti metal and compact TiO_2 films, the XRD diffraction peaks (Figure 2B) at $2\theta = 36.08°$, $41.21°$, $54.57°$ and $62.86°$ were observed, corresponding to those of lattice planes (101), (111), (211) and (002) of rutile TiO_2 phase (JCPDS No. 88-1875).

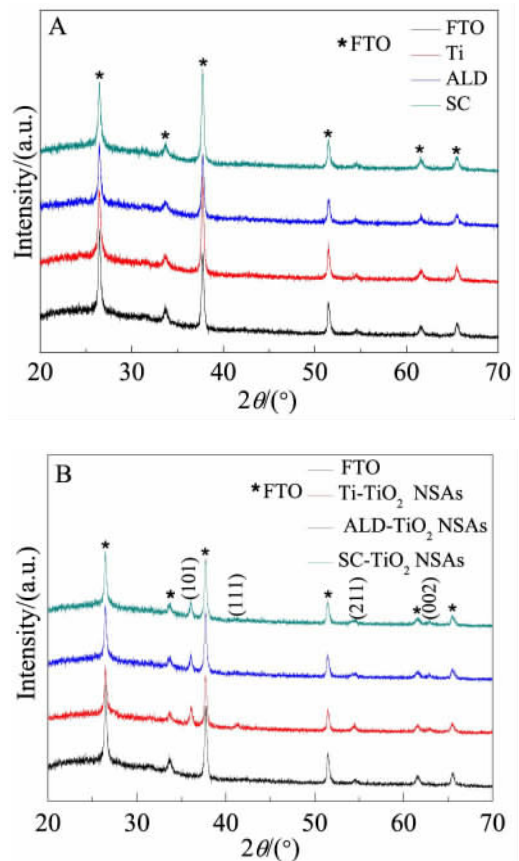Figure 3(A-F) exhibits SEM images of the rutile TiO_2 NSA films indexed by XRD patterns in Figure

Fig. 2 XRD patterns of the Ti metal and compact TiO_2 layers(A), and TiO_2 NSAs (B) grown on the pre-treated FTO substrates via hydrothermal reaction in 60 mL aqueous solution (pH = 0.85) with $TiCl_3$ (0.8 mL 15 wt% of $TiCl_3$ in H_2O and HCl solution) at 80 °C for 4 h.

2B. As shown in Figures 2A and 2B, the Ti metal layer-based TiO_2 (abbreviated as Ti-TiO_2) film with a 450 °C-heating post-treatment consisted of well-de fined nanosheet arrays and the vertical TiO_2 nanosheets randomly but uniformly grew on the FTO substrate. It was observed that the TiO_2 NSAs possessed a sheet thickness of $\sim$ 30 nm (Figure 3A) and a film thickness of $\sim$ 550 nm (Figure 3B). More intriguing, the color of the as-prepared sample still kept brown green (the left inset in Figure 3A), implying the coexistence of Ti metal and TiO_2 NSAs. However, this brown green color was turned into white and translucent (the right inset in Figure 3A) after the 450 °C-heating post-treatment. It was demonstrated that the thermal treat-ment not only increased the crystallinity of TiO_2 NSAs, but also transformed the Ti metal layer into a

compact TiO$_2$ layer. Such compact layer with the thickness of ~100 nm could be obviously observed between the TiO$_2$ NSAs and the FTO substrate (Figure 3B). For the TiO$_2$ NSAs grown on the compact TiO$_2$ layer prepared from the ALD method (abbreviated as ALD-TiO$_2$ NSAs), different film features could be seen, that is, many nanosheet building blocks aggregated into a flower-like architecture which randomly dispersed over a compact layer on the FTO substrate (Figure 3C). In addition, the film surface was uneven with a maximum thickness of ~450 nm (Figure 3D) and the film color was white (the inset in Figure 3C). For the TiO$_2$ NSAs grown on the compact TiO$_2$ layer prepared from the SC method (abbreviated as SC-TiO$_2$ NSAs), similar nanosheet arrays were also successfully planted on the FTO substrate (Figure 3E). Nevertheless, the film flatness and

uniformity of the SC-TiO$_2$ NSAs (Figure 3E) were slightly worse than those of the Ti-TiO$_2$ NSAs (Figure 3A). Analogously, the film color of the 600 nm-thick SC-TiO$_2$ NSAs (Figure 3F) was white as well (the inset in Figure 3E). Remarkably, the pre-treatment of the Ti metal or compact TiO$_2$ layers on the FTO substrates played a heavy impact on the shape of the hydrothermal films. It was predicted that the superior orientation and uniformity of the Ti-TiO$_2$ NSAs would make them more efficient as scaffold materials in PSCs.

To further study the detailed structures of the Ti-TiO$_2$ NSAs, TEM analysis was subsequently carried out. The obtained TEM image also revealed that the piece scratched off the Ti-TiO$_2$ NSA sample exhibited a nanosheet feature (Figure 3G). And this nanosheet was completely crystalline as proved by the
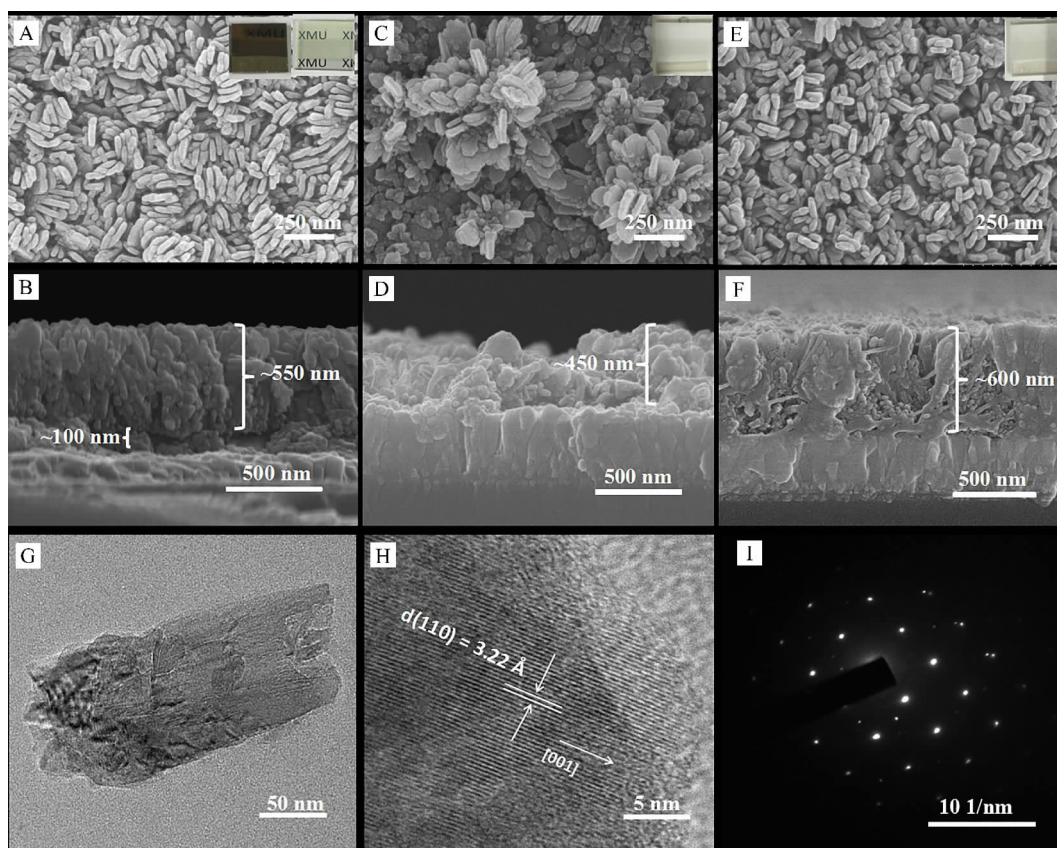

Fig. 3 SEM images of top view (A, C, E) and cross-sectional view (B, D, F) of the TiO$_2$ NSAs based on the (A, B) Ti metal layer, (C, D) ALD and (E, F) SC prepared compact TiO$_2$ layers. Insets are their corresponding real photos. The left insets in (A) is the sample without annealing, while the right one is the sample with annealing at 450 °C for 2 h. (G) TEM and (H) HRTEM images, and (I) the corresponding SAED pattern image of the TiO$_2$ NSAs based on the Ti metal layer.
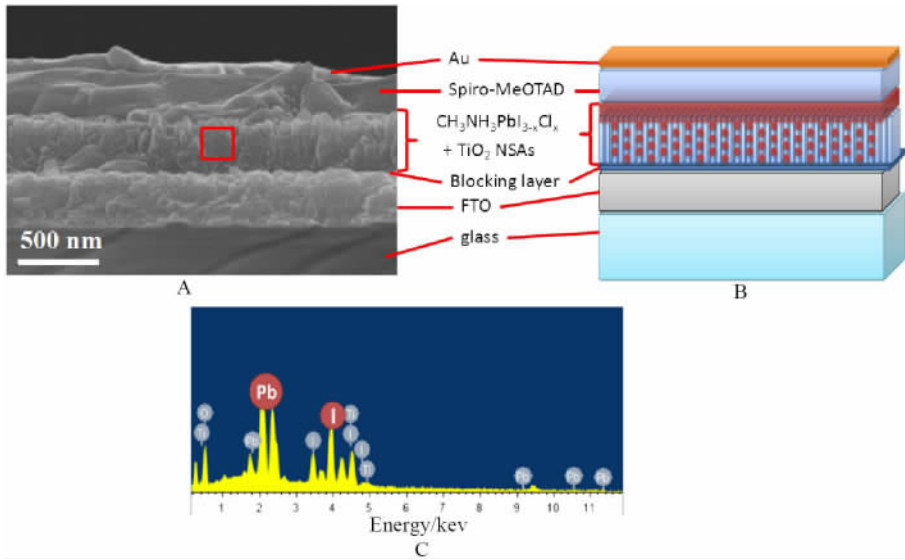
Fig. 4 A. Cross-sectional SEM image of a full PSC device based on the Ti-TiO$_2$ NSAs; B. Schematic representation of full device structure (A), and C. EDS plot of the part marked in (A) using a red square

HRTEM image, in which lattice fringe with interplanar spacing, d_{110} = 0.322 nm, can be indexed to rutile TiO$_2$ phase with the preferential growth along the [001] direction (Figure 3H). The corresponding SAED pattern of the Ti-TiO$_2$ NSAs indicated that it was single crystal with well crystallinity (Figure 3I).

The Ti/ALD/SC-TiO$_2$ NSAs grown on FTO substrates (Figure 3(A-F)) were then applied as scaffold materials to assemble PSCs with CH$_3$NH$_3$PbI$_{3-x}$Cl$_x$ as light harvester, spiro-MeOTAD as HTM, and a Au film as back contact (Figure 4(A-B)). Significantly, the EDS plot (Figure 4C) of the part marked with a red square in Figure 4A suggested that the CH$_3$NH$_3$PbI$_{3-x}$Cl$_x$ perovskite had penetrated into the Ti-TiO$_2$ NSAs which was beneficial to the electron transport from the perovskite to the scaffold layer.

Table 1 summarizes the photovoltaic parameters of the resulting PSCs and Figure 5 shows the corresponding current-voltage (J-V) characteristics. Compared with the ALD/SC-TiO$_2$ NSAs, greatly enhanced photovoltaic performance of the PSCs employing Ti-TiO$_2$ NSAs as the scaffold materials was finally achieved (Table 1 and Figure 5). It was demonstrated that the Ti-TiO$_2$ NSAs contributed the device with higher short circuit current density (J_{sc}; Ti: 13.41 mA·cm^{-2} vs. ALD: 11.68 mA·cm^{-2} and SC: 12.00
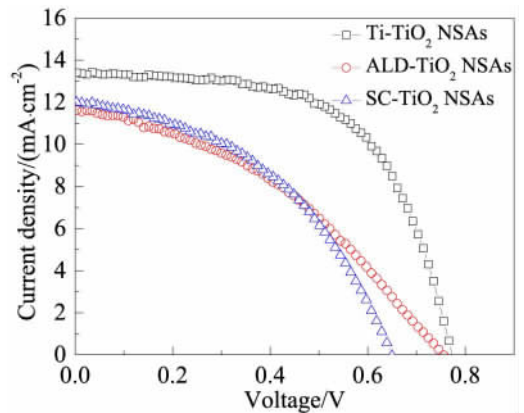

Fig. 5 J-V curves of the PSCs based on the Ti/ALD/SC-TiO$_2$ NSAs

mA·cm^{-2}), open circuit voltage (V_{oc}; Ti: 0.77 V vs. ALD: 0.75 V and SC: 0.65 V) and fill factor (FF; Ti: 59.85% vs. ALD: 38.74% and SC: 44.26%), and thus, remarkably improved power conversion efficiency (PCE; Ti: 6.20% vs. ALD: 3.39% and SC: 3.45%) for the assembling PSC (Table 1 and Figure 5). Therefore, it was indicated that the Ti-TiO$_2$ NSAs had better properties for the electron transport because of the higher orientation and uniformity of the nanosheet arrays, in combination with the close connection of the FTO/compact TiO$_2$ layer/rutile TiO$_2$ NSAs, consequently reflecting a largely reduced series resistance of the device (R; Ti: 69.82 Ω vs. ALD: 411.59 Ω and

Tab. 1 Photovoltaic parameters of the PSCs based on the Ti/ALD/SC-TiO$_2$ NSAs

Sample	J_{sc}/(mA·cm^{-2})	V_{oc}/V	FF/%	PCE/%	R at V_{oc}/Ω
Ti-TiO$_2$ NSAs	13.41	0.77	59.85	6.20	69.82
ALD-TiO$_2$ NSAs	11.68	0.75	38.47	3.39	411.59
SC-TiO$_2$ NSAs	12.00	0.65	44.26	3.45	190.37

SC: 190.37 Ω).

In order to further improve the PCEs of the Ti-TiO$_2$ NSA-based PSCs, several modification processes were carried out. First of all, the hydrothermal condition for the growth of the Ti-TiO$_2$ NSAs was optimized, including the solution pH value and the volume of TiCl$_3$ precursor. It was found that they both played obvious impact on the morphologies of the TiO$_2$ NSAs, and finally showed different PCEs in PSC application (Table 2). The optimized conditions were 1.05 and 0.6 mL for the solution pH value (Table 2) and the volume of TiCl$_3$ precursor (Table 2), respectively. In addition, the TiCl$_4$ post-treatment time was chosen as well, and 0.5 h was found to be the most effective time (Table 2).

Besides, it is well-known that CH$_3$NH$_3$PbI$_{3-x}$Cl$_x$ perovskite is very sensitive to humid condition, and then the Ti-TiO$_2$ NSA-based PSCs were fabricated in glove box and air condition (humidity: 60 ~ 70%), re-

spectively. It was indicated that the perovskite film prepared in glove box was fully and uniformly covered on top of the Ti-TiO$_2$ NSAs (Figure 6A), while the coverage of the perovskite film directly prepared in air condition was incomplete (Figure 6B), and such perovskite film had inferior crystallinity to the one prepared in glove box (Figure 6C). More seriously, the color of the PSC device stored in air condition was quickly faded (Figure 6D), implying the deterioration of its perovskite film. And the device preserved in glove box kept stable (Figure 6E). The resulting Ti-TiO$_2$ NSA-based PSC prepared in glove box exhibited more significantly enhanced performance than that organized in air condition (Figure 6 (F-G) and Table 2).

Finally, the method for the perovskite deposition was also examined. One step spin coating, two-step dipping, and two-step spin coating methods were used (See Experimental Section) to deposit CH$_3$NH$_3$PbI$_{3-x}$Cl$_x$ per

Tab. 2 Photovoltaic parameters of the PSCs based on the Ti-TiO$_2$ NSAs prepared under different conditions

| Parameter		J_{sc}/(mA·cm^{-2})	V_{oc}/V	FF/%	PCE/%
Solution pH	0.75	12.17	0.78	61.36	5.84
	0.85	13.41	0.77	59.85	6.20
	1.05	16.70	0.79	53.83	7.14
TiCl$_3$ volume/mL	0.5	21.18	0.73	52.94	8.21
	0.6	18.39	0.76	61.54	8.53
	0.8	16.70	0.79	53.83	6.36
TiCl$_4$ treatment time/h	0	21.18	0.73	52.94	8.21
	0.5	21.02	0.73	56.02	8.59
	1	19.12	0.72	46.20	7.14
Device organization condition	Glove box	18.39	0.76	61.54	8.59
	Air (humidity: 70 ~ 90%)	13.46	0.68	40.32	3.67
Other perovskite deposition method	Two-step (dipping)	5.08	0.83	80.25	3.37
	Two-step (spin coating)	7.39	0.92	35.11	2.40
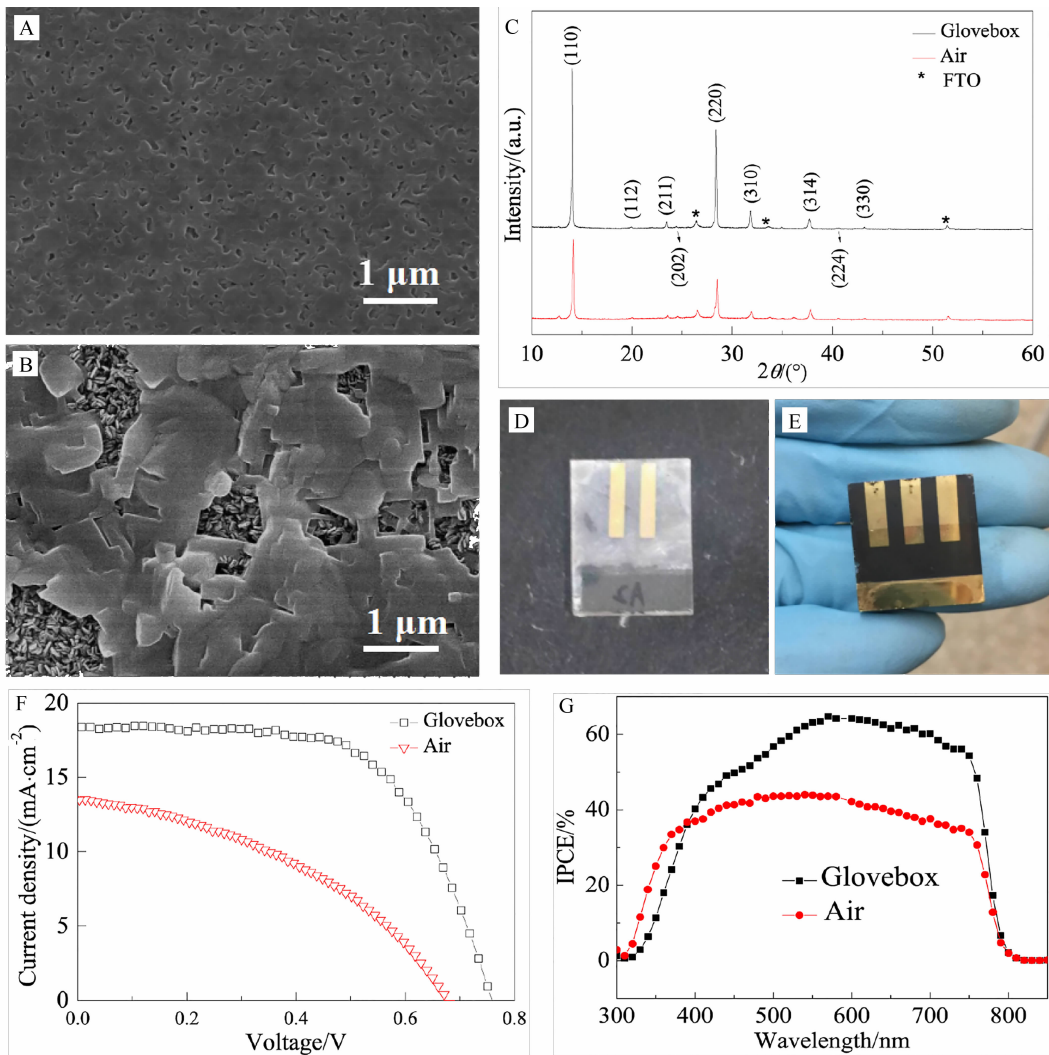
Fig. 6 SEM images (A, B) of top view and XRD patterns (C) of the Ti-TiO$_2$ NSA-based perovskite films prepared in glove box (A) and air condition (humidity: 60 ~ 70%) (B), respectively. Real photos of the Ti-TiO$_2$ NSA-based PSC devices stored in air condition (humidity: 60 ~ 70%) (D) and glove box (E) for 3 h, respectively. *J-V* curves (F) and IPCE plots (G) of the Ti-TiO$_2$ NSA-based PSCs prepared in glove box and air condition (humidity: 60 ~ 70%).

ovskite over the Ti-TiO$_2$ NSAs. It was revealed that the film quality deposited by one step spin coating was better than the other two methods, and the superior cell performance (Table 3) also further proved that one step spin coating method was more efficient to deposit CH$_3$NH$_3$PbI$_{3-x}$Cl$_x$ film on top of the Ti-TiO$_2$ NSAs.

Combined with all the above factors, the Ti-TiO$_2$ NSA-based PSC device was undergone continuous modification and then its PCE was improved step by step (Figure 7). Impressively, the best PCE value of 11.82% with the J_{sc} value of 21.03 mA·cm^{-2}, V_{oc}

value of 0.90 V, and FF value of 62.26% (Figure 7) was finally achieved.

3 Conclusions

The Ti metal layer assisted-hydrothermal process has been firstly exploited to construct the vertical rutile TiO$_2$ NSAs directly grown on FTO substrates. The subsequent heating treatment converted such Ti metal layers into compact TiO$_2$ layers with well connection between the rutile TiO$_2$ NSAs and the FTO substrates. The resulting novel compact TiO$_2$ layer in combination with the oriented rutile TiO$_2$ NSAs exhibited a highest PCE of 11.82% when ap-
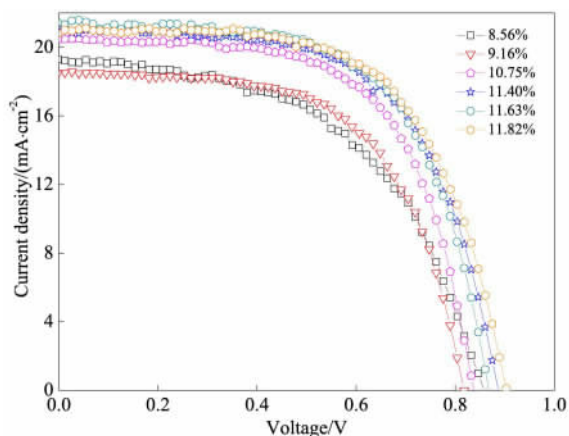
Fig. 7 *J-V* curves of the Ti-TiO$_2$ NSA-based PSC devices with careful modification and continuously improved PCEs

plied in PSCs after careful modification. Such synthesis strategy presented a facile but an effective way to develop a high-quality TiO$_2$ compact layer with close contacts between the TiO$_2$ scaffold and the conductive substrate for the efficient PSCs.

Acknowledgements

References:

[1] Serrano E, Rus G, García-Martínez J. Nanotechnology for sustainable energy[J]. Renewable & Sustainable Energy Reviews, 2009, 13(9): 2373-2384.

[2] Park N G. Perovskite solar cells: An emerging photovoltaic technology[J]. Materials Today, 2015, 18(2): 65-72.

[3] Gratzel M. The light and shade of perovskite solar cells[J]. Nature Materials, 2014, 13(9): 838-842.

[4] McGehee M D. Perovskite solar cells: Continuing to soar[J]. Nature Materials, 2014, 13(9): 845-846.

[5] Hodes G, Cahen D. Photovoltaics: Perovskite cells roll forward[J]. Nature Photonics, 2014, 8(2): 87-88.

[6] Green M A, Bein T. Photovoltaics Perovskite cells charge forward[J]. Nature Materials, 2015, 14(6): 559-561.

[7] Park N G. Perovskite solar cells switchable photovoltaics[J]. Nature Materials, 2015, 14(2): 140-141.

[8] Green M A, Ho-Baillie A, Snaith H J. The emergence of perovskite solar cells[J]. Nature Photonics, 2014, 8(7): 506-514.

[9] Hodes G. Perovskite-based solar cells[J]. Science, 2013, 342(6156): 317-318.

[10] Kojima A, Teshima K, Shirai Y, et al. Organometal halide perovskites as visible-light sensitizers for photovoltaic cells[J]. Journal of the American Chemical Society, 2009, 131(17): 6050-6051.

[11] Best research-cell efficiencies NREL (2016)[EB/OL]. Best research-cell efficiencies NREL (2016): www.nrel.gov/ncpv/images/efficiency_chart.jpg.

[12] Tan K W, Moore D T, Saliba M, et al. Thermally induced structural evolution and performance of mesoporous block copolymer-directed alumina perovskite solar cells[J]. ACS Nano, 2014, 8(5): 4730-4739.

[13] Deng Y H, Peng E, Shao Y C, et al. Scalable fabrication of efficient organolead trihalide perovskite solar cells with doctor-bladed active layers[J]. Energy & Environmental Science, 2015, 8(5): 1544-1550.

[14] Law C, Miseikis L, Dimitrov S, et al. Performance and stability of lead perovskite/TiO$_2$, polymer/PCBM, and dye sensitized solar cells at light intensities up to 70 suns[J]. Advanced Materials, 2014, 26(36): 6268-6273.

[15] Park B W, Philippe B, Gustafsson T, et al. Enhanced crystallinity in organic-inorganic lead halide perovskites on mesoporous TiO$_2$ via disorder-order phase transition[J]. Chemistry of Materials, 2014, 26(15): 4466-4471.

[16] Im J H, Luo J S, Franckevicius M, et al. Nanowire perovskite solar cell[J]. Nano Letters, 2015, 15(3): 2120-2126.

[17] Yantara N, Sabba D, Yanan F, et al. Loading of mesoporous titania films by CH$_3$NH$_3$PbI$_3$ perovskite, single step vs. sequential deposition[J]. Chemical Communications, 2015, 51(22): 4603-4606.

[18] Xie F X, Zhang, D, Su H M, et al. Vacuum-assisted thermal annealing of CH$_3$NH$_3$PbI$_3$ for highly stable and efficient perovskite solar cells[J]. ACS Nano, 2015, 9(1): 639-646.

[19] Bi D Q, El-Zohry A M, Hagfeldt A, et al. Unraveling the effect of PbI$_2$ concentration on charge recombination kinetics in perovskite solar cells[J]. ACS Photonics, 2015, 2(5): 589-594.

[20] Zhang T Y, Yang M J, Zhao Y X, et al. Controllable sequential deposition of planar CH$_3$NH$_3$PbI$_3$ perovskite films via adjustable volume expansion[J]. Nano Letters, 2015, 15(6): 3959-3963.

[21] Cai B, Xing Y D, Yang Z, et al. High performance hybrid solar cells sensitized by organolead halide perovskites[J]. Energy & Environmental Science, 2013, 6(5): 1480-1485.

[22] Leijtens T, Eperon G E, Pathak S, et al. Overcoming ultraviolet light instability of sensitized TiO₂ with meso-su perstructured organometal tri-halide perovskite solar cells[J]. Nature Communications, 2013, 4: 2885.

[23] Moehl T, Im J H, Lee Y H, et al. Strong photocurrent amplification in perovskite solar cells with a porous TiO₂ blocking layer under reverse bias[J]. The Journal of Physical Chemistry Letters, 2014, 5(21): 3931-3936.

[24] Jena A K, Chen H W, Kogo A, et al. The interface between FTO and the TiO₂ compact layer can be one of the origins to hysteresis in planar heterojunction perovskite solar cells[J]. ACS Applied Materials & Interfaces, 2015, 7(18): 9817-9823.

[25] Suarez B, Gonzalez-Pedro V, Ripolles T S, et al. Recombination study of combined halides (Cl, Br, I) perovskite solar cells[J]. The Journal of Physical Chemistry Letters, 2014, 5(10): 1628-1635.

[26] Bi D Q, Moon S J, Haggman L, et al. Using a two-step deposition technique to prepare perovskite (CH₃NH₃PbI₃) for thin film solar cells based on ZrO₂ and TiO₂ mesostructures[J]. RSC Advances, 2013, 3(41): 18762-18766.

[27] Xiao J Y, Shi J J, Liu H B, et al. Efficient CH₃NH₃PbI₃ perovskite solar cells based on graphdiyne (GD)-modified P₃HT hole-transporting material[J]. Advanced Energy Materials, 2015, 5(8): 1401943.

[28] Heo J H, Im S H, Noh J H, et al. Efficient inorganic-organic hybrid heterojunction solar cells containing perovskite compound and polymeric hole conductors[J]. Nature Photonics, 2013, 7(6): 487-492.

[29] Abrusci A, Stranks S D, Docampo P, et al. High-performance perovskite-polymer hybrid solar cells via electronic coupling with fullerene monolayers[J]. Nano Letters, 2013, 13(7): 3124-3128.

[30] Jeng J Y, Chiang Y F, Lee M H, et al. CH₃NH₃PbI₃ perovskite/fullerene planar-heterojunction hybrid solar cells[J]. Advanced Materials, 2013, 25(27): 3727-3732.

[31] Kuang C Y, Tang G, Jiu T G, et al. Highly efficient electron transport obtained by doping PCBM with graphdiyne in planar-heterojunction perovskite solar cells[J]. Nano Letters, 2015, 15(4): 2756-2762.

[32] Marinova N, Tress W, Humphry-Baker R, et al. Light harvesting and charge recombination in CH₃NH₃PbI₃ perovskite solar cells studied by hole transport layer thickness variation[J]. ACS Nano, 2015, 9(4): 4200-4209.

[33] Azimi H, Ameri T, Zhang H, et al. A universal interface layer based on an amine-functionalized fullerene derivative with dual functionality for efficient solution processed organic and perovskite solar cells[J]. Advanced Energy Materials, 2015, 5(8): 1401692.

[34] Kim H S, Lee C R, Im J H, et al. Lead iodide perovskite sensitized all-solid-state submicron thin film mesoscopic solar cell with efficiency exceeding 9%[J]. Scientific Reports, 2012, 2: 591-598.

[35] Liu M Z, Johnston M B, Snaith H J. Efficient planar heterojunction perovskite solar cells by vapour deposition[J]. Nature, 2013, 501(7467): 395-398.

[36] Shi S W, Li Y F, Li X Y, et al. Advancements in all-solid-state hybrid solar cells based on organometal halide perovskites[J]. Materials Horizons, 2015, 2(4): 378-405.

[37] Yang W S, Noh J H, Jeon N J, et al. High-performance photovoltaic perovskite layers fabricated through intramolecular exchange[J]. Science, 2015, 348(6240): 1234-1237.

[38] Xiao Y M, Han G Y, Li Y P, et al. Preparation of high performance perovskite-sensitized nanoporous titanium dioxide photoanodes by *in situ* method for use in perovskite solar cells[J]. Journal of Materials Chemistry A, 2014, 2(39): 16531-16537.

[39] Xiao Y M, Han G Y, Chang Y Z, et al. Investigation of perovskite-sensitized nanoporous titanium dioxide photoanodes with different thicknesses in perovskite solar cells[J]. Journal of Power Sources, 2015, 286: 118-123.

[40] Qin P, Tanaka S, Ito S, et al. Inorganic hole conductor-based lead halide perovskite solar cells with 12.4% conversion efficiency[J]. Nature Communications, 2014, 5: 3834.

[41] Giacomo F D, Zardetto V, D'Epifanio A, et al. Flexible perovskite photovoltaic modules and solar cells based on atomic layer deposited compact layers and UV-irradiated TiO₂ scaffolds on plastic substrates[J]. Advanced Energy Materials, 2015, 5(8): 1401808.

[42] Wu Y Z, Yang X D, Chen H, et al. Highly compact TiO₂ layer for efficient hole-blocking in perovskite solar cells[J]. Applied Physics Express, 2014, 7(5): 052301.

[43] Gao Q Q, Yang S W, Lei L, et al. An effective TiO₂ blocking layer for perovskite solar cells with enhanced performance[J]. Chemistry Letters, 2015, 44(5): 624-626.

[44] Do Sung S, Kang M S, Choi I T, et al. 14.8% perovskite solar cells employing carbazole derivatives as hole transporting materials[J]. Chemical Communications, 2014, 50(91): 14161-14163.

[45] Krishnamoorthy T, Kunwu F, Boix P P, et al. A swivel-cruciform thiophene based hole-transporting material for

efficient perovskite solar cells[J]. Journal of Materials Chemistry A, 2014, 2(18): 6305-6309.

[46] Do K, Choi H, Lim K, et al. Star-shaped hole transporting materials with a triazine unit for efficient perovskite solar cells[J]. Chemical Communications, 2014, 50(75): 10971-10974.

[47] Qin P, Tetreault N, Dar M I, et al. A novel oligomer as a hole transporting material for efficient perovskite solar cells[J]. Advanced Energy Materials, 2014, 5(2): 1400980.

[48] Zhu Z L, Bai Y, Lee H K H, et al. Polyfluorene derivatives are high-performance organic hole-transporting ma terials for inorganic-organic hybrid perovskite solar cells[J]. Advanced Functional Materials, 2014, 24(46): 7357-7365.

[49] Fu N Q, Huang C, Liu Y, et al. Organic-free anatase TiO_2 paste for efficient plastic dye-sensitized solar cells and low temperature processed perovskite solar cells[J]. ACS Applied Material & Interfaces, 2015, 7(34): 19431-19438.

[50] Kim H S, Lee J W, Yantara N, et al. High efficiency solid-state sensitized solar cell-based on submicrometer rutile TiO_2 nanorod and $CH_3NH_3PbI_3$ perovskite sensitizer [J]. Nano Letters, 2013, 13(6): 2412-2417.

[51] Qiu J H, Qiu Y C, Yan K Y, et al. All-solid-state hybrid solar cells based on a new organometal halide perovskite sensitizer and one-dimensional TiO_2 nanowire arrays[J]. Nanoscale, 2013, 5(8): 3245-3248.

[52] Jiang Q L, Sheng X, Li Y X, et al. Rutile TiO_2 nanowire-based perovskite solar cells[J]. Chemical Communications, 2014, 50(94): 14720-14723.

[53] Cai B, Zhong D, Yang Z, et al. An acid-free medium gro-wth of rutile TiO_2 nanorods arrays and their application in perovskite solar cells[J]. Journal of Materials Chemistry C, 2015, 3(4): 729-733.

[54] Fakharuddin A, Giacomo F D, Ahmed I, et al. Role of morphology and crystallinity of nanorod and planar electron transport layers on the performance and long term durability of perovskite solar cells[J]. Journal of Power Sources, 2015, 283: 61-67.

[55] Mali S S, Shim C S, Park H K, et al. Ultrathin atomic lay-er deposited TiO_2 for surface passivation of hydrothermally grown 1D TiO_2 nanorod arrays for efficient sol-id-state perovskite solar cells[J]. Chemical Materials, 2015, 27(5): 1541-1551.

[56] Zhong D, Cai B, Wang X L, et al. Synthesis of oriented TiO_2 nanocones with fast charge transfer for perovskite solar cells[J]. Nano Energy, 2015, 11: 409-418.

[57] Cai B, Zhong D, Yang Z, et al. An acid-free medium

growth of rutile TiO_2 nanorods arrays and their applica-tion in perovskite solar cells[J]. Journal of Materials Chemistry C, 2015, 3(4): 729-733.

[58] Gao X F, Li J Y, Baker J, et al. Enhanced photovoltaic performance of perovskite $CH_3NH_3PbI_3$ solar cells with freestanding TiO_2 nanotube array films[J]. Chemical Co-mmunications, 2014, 50(48): 6368-6371.

[59] Wang X Y, Li Z, Xu W J, et al. TiO_2 nanotube arrays based flexible perovskite solar cells with transparent car-bon nanotube electrode[J]. Nano Energy, 2015, 11: 728-735.

[60] Dharani S, Mulmudi H K, Yantara N, et al. High efficien-cy electrospun TiO_2 nanofiber based hybrid organic-inor-ganic perovskite solar cell[J]. Nanoscale, 2014, 6(3): 1675-1679.

[61] Zhong D, Cai B, Wang X L, et al. Synthesis of oriented TiO_2 nanocones with fast charge transfer for perovskite solar cells[J]. Nano Energy, 2015, 11: 409-418.

[62] Rong Y G, Ku Z L, Mei A, et al. Hole-conductor-free mesoscopic $TiO_2/CH_3NH_3PbI_3$ heterojunction solar cells based on anatase nanosheets and carbon counter elec-trodes[J]. The Journal of Physical Chemistry Letters, 2014, 5(12): 2160-2164.

[63] Dar M I, Ramos F J, Xue Z S, et al. Photoanode based on (001)-oriented anatase nanoplatelets for organic-inorgan-ic lead iodide perovskite solar cell[J]. Chemistry of Mate-rials, 2014, 26(16): 4675-4678.

[64] Lee J W, Lee S H, Ko H S, et al. Opto-electronic proper-ties of TiO_2 nanohelices with embedded HC $(NH_2)_2PbI_3$ perovskite solar cells[J]. Journal of Materials Chemistry A, 2015, 3(17): 9179-9186.

[65] Wu W Q, Huang F Z, Chen D H, et al. Thin films of den-dritic anatase titania nanowires enable effective hole-blocking and efficient light-harvesting for high-per-formance mesoscopic perovskite solar cells[J]. Advanced Functial Materials, 2015, 25(21): 3264-3272.

[66] Sun H X, Ruan P, Bao Z q, et al. Shell-in-shell TiO_2 hol-low microspheres and optimized application in light-trap-ping perovskite solar cells[J]. Solid State Sciences, 2015, 40: 60-66.

[67] Mahmood K, Swain B S, Amassian A. Highly efficient hybrid photovoltaics based on hyperbranched three-di mensional TiO_2 electron transporting materials [J]. Ad-vanced Materials, 2015, 27(18): 2859-2865.

[68] Wu Y Z, Yang X D, Chen H, et al. Highly compact TiO_2 layer for efficient hole-blocking in perovskite solar cells[J]. Applied Physics Express, 2014, 7(5): 052301.

1a   1a   1   1,2*

(1.   ,   ,   ,   361005；2.   ,

,   ,   ,   ,   361005）

：   ，   FTO   Ti   ，   ， TiO_2

（TiO_2 NSAs）.   ，Ti TiO_2 ， TiO_2 NSAs

FTO   .   (ALD)   (SC) TiO_2 TiO_2

NSAs   ， TiO_2 NSAs   .

TiO_2 NSAs   ， TiO_2 NSAs/TiO_2 /FTO   .   ，

， TiO_2 NSAs   11.82%.

： Ti   ；TiO_2 ；